Author Manuscript

Ionizing radiation-induced acoustics for radiotherapy and diagnostic radiology applications

Susannah Hickling

Corresponding author: susannah.hickling@mail.mcgill.ca

Department of Physics & Medical Physics Unit, McGill University,

1001 boul Decarie, Montreal, QC, H4A 3J1, Canada

Liangzhong Xiang

School of Electrical and Computer Engineering,

University of Oklahoma, Norman, OK, 73019, USA

Kevin C. Jones

Department of Radiation Oncology,

Rush University Medical Center, Chicago, IL, 60612, USA

Katia Parodi and Walter Assmann

Department of Medical Physics, Ludwig-Maximilians-Universität München,

Garching b. München, 85748, Germany

Stephen Avery

Department of Radiation Oncology,

University of Pennsylvania, Philadelphia, PA, 19104, USA

Maritza Hobson

Medical Physics Unit, McGill University Health Center; Department of Oncology,

Department of Physics- Medical Physics Unit,

McGill University, Montreal, QC, H4A 3J1,Canada

Issam El Naqa

Department of Radiation Oncology,

University of Michigan, Ann Arbor, MI, 48103-4943, USA

1

Abstract

Acoustic waves are induced via the thermoacoustic effect in objects exposed to a pulsed beam of ionizing radiation. This phenomenon has interesting potential applications in both radiotherapy dosimetry and treatment guidance as well as low dose radiological imaging. After initial work in the field in the 1980s and early 1990s, little research was done until 2013 when interest was rejuvenated, spurred on by technological advances in ultrasound transducers and the increasing complexity of radiotherapy delivery systems. Since then, many studies have been conducted and published applying ionizing radiation-induced acoustic principles into three primary research areas: Linear accelerator photon beam dosimetry, proton therapy range verification, and radiological imaging. This review article introduces the theoretical background behind ionizing radiation-induced acoustic waves, summarizes recent advances in the field, and provides an outlook on how the detection of ionizing radiation-induced acoustic waves can be used for relative and *in vivo* dosimetry in photon therapy, localization of the Bragg peak in proton therapy, and as a low-dose medical imaging modality. Future prospects and challenges for clinical implementation of these techniques are discussed.

Keywords: radiation acoustics, photon beam dosimetry, proton range verification, low dose imaging

I. INTRODUCTION

Alexander Graham Bell discovered the thermoacoustic effect in 1880 while working on his invention of the photophone, a device to transmit sound via a beam of light, when he observed that acoustic waves were generated when a solid sample was exposed to a rapidly interrupted beam of sunlight [1]. This phenomenon whereby acoustic waves are induced following a pulse of electromagnetic radiation is commonly referred to as the photoacoustic effect, however this implies that only photon beams are capable of generating acoustic waves. Since the induction of acoustic waves is observed after irradiation by a pulsed beam of charged or uncharged particles, the term thermoacoustic effect is more general and will be used throughout this article.

Briefly, the thermoacoustic effect can be summarized as follows. When a pulsed beam of high energy radiation strikes a material the localized temperature increase leads to thermoelastic expansion and the build up of a differential pressure distribution, which is dependent on the properties of the material as well as the radiation beam. This causes the propagation of acoustic pressure waves that can be detected using devices such as ultrasound transducers and hydrophones, which typically use piezoelectric crystals to generate an electrical signal in response to mechanical stress/pressure. Information regarding the pressure distribution induced following a pulse of radiation can be extracted from the detected time-varying pressure signals, and an image of the initial differential pressure distribution can be reconstructed using signals acquired at multiple angles surrounding the irradiated region.

The thermoacoustic effect has been widely studied and applied to medicine as early as the 1980s when it was proposed that it could be exploited to image tissue [2]. This idea gave rise to photoacoustic imaging, which uses optical photons from a laser source to induce acoustic waves. Contrast in photoacoustic imaging arises from the differential absorption of optical photons in the body, thus structures such as hemoglobin, lipids and melanin can be imaged [3]. Photoacoustic imaging has been widely used as a preclinical imaging technique and has recently been translated to the clinic, primarily for superficial applications such as breast cancer imaging [4]. Similarly, the term thermoacoustic imaging refers to an imaging modality that uses a pulsed microwave source to image tissues based on their dielectric properties. While it has been applied to cancer imaging, microwave thermoacoustic imaging is less widespread than photoacoustic imaging [5]. Although both are rapidly advancing,

photoacoustic techniques are limited by the penetration depth of optical photons, while microwave thermoacoustic imaging is often hindered by poor dielectric contrast.

The goal of this article is to explore how the detection of the acoustic waves induced by ionizing radiation beams can be applied in radiation therapy and diagnostic radiology. As early as 1981, it was proposed that detecting the acoustic waves generated by therapeutic radiation beams could serve as a means for verifying treatment delivery [2]. While promising work was done in this area in the 1980s and early 1990s, few studies were published between that time and 2013, when interest in the field was renewed. Since 2013, ionizing radiation-induced acoustics has been applied to three main areas: (1) linear accelerator (linac) photon beam dosimetry; (2) proton therapy range verification; and (3) medical imaging. Many studies have been published in recent years demonstrating the feasibility and potential of using ionizing radiation-induced acoustics in these three areas. It is now time to work on translating these promising initial studies into clinically viable techniques. All three applications of ionizing radiation-induced acoustics share the same physics principles, thus advancements in one application are highly relevant to the others.

This article provides a future outlook of the field of radiation-induced acoustics for radiotherapy and diagnostic radiology applications and is divided into three focus areas:

1. Linac photon beam dosimetry

2. Proton therapy range verification

3. Medical imaging.

The article begins with an initial background review of the theory behind ionizing radiation-induced acoustics and initial studies in the field that have motivated recent work in the above three areas.

II.   THEORY

The thermoacoustic effect states that acoustic waves are induced in an object following a pulse of irradiation. The sections below detail how a beam of ionizing radiation deposits dose and heat energy within an object, and how this leads to a temperature rise, thermoelastic expansion, and ultimately the generation and propagation of acoustic waves throughout the

₈₅ irradiated object. The ability to reconstruct images based on the detection of these acoustic
₈₆ waves is also discussed.

A. Deposition of dose by ionizing radiation

₈₈ The primary quantity of interest in radiation therapy is radiation dose, which is defined as
₈₉ the amount of energy deposited per unit mass by a beam of ionizing radiation and quantified
₉₀ using the unit Gray (1 Gray=1 Joule/kg). Beams of charged particles, such as protons or
₉₁ electrons, are considered directly ionizing radiation since they deposit their energy through
₉₂ Coulombic interactions within the media they traverse. Beams of uncharged particles, such
₉₃ as photons, are classified as indirectly ionizing radiation since they must undergo interactions
₉₄ to release secondary charged particles which then deposit their energy through Coulombic
₉₅ interactions.

₉₆ Due to the stochastic nature of energy deposition, Monte Carlo (MC) techniques are
₉₇ considered to be the most accurate way of calculating radiation dose [6]. MC techniques
₉₈ simulate particle trajectories using random numbers to sample the probability density func-
₉₉ tions of potential interactions a particle may undergo as it traverses a medium. A number of
₁₀₀ MC codes are used for radiation therapy dose calculation applications, including egsNRC [7],
₁₀₁ Geant4 [8], MCNP [9], Fluka [10] and PENELOPE [11]. MC techniques are commonly used
₁₀₂ in ionizing radiation-induced acoustics simulations to obtain the dose distribution following
₁₀₃ a pulse of radiation.

B. Heat energy and temperature increase

₁₀₅ Nearly all of the energy deposited by a beam of ionizing radiation is converted to heat
₁₀₆ energy. The heat defect, which is dependent on the type of ionizing radiation and material
₁₀₇ being irradiated, refers to the amount of energy not deposited as heat energy, and therefore
₁₀₈ does not contribute to a temperature increase. Chemical reactions are the primary contrib-
₁₀₉ utor to the heat defect, with exothermic reactions leading to a heat defect less than zero
₁₁₀ and endothermic reactions resulting in a positive heat defect. A small amount of energy
₁₁₁ also goes into radiation-induced acoustic and optical emissions [12]. The heat defect, k_{HD},
₁₁₂ is related to deposited ionizing radiation dose, D, through:

$$D = \frac{E}{m} = \frac{E_H}{(1 - k_{HD})m}, \tag{1}$$

[113] where E is the total energy deposited in a volume of mass m, and E_H is the deposited [114] heat energy.

[115] Assuming that the heat energy is deposited in a shorter time than it takes the density [116] or volume of the irradiated medium to change, the deposition of heat energy results in a [117] temperature rise, ΔT, given by:

$$\Delta T = \frac{H}{\rho_0 \cdot C_v}, \tag{2}$$

[118] where H is the heat energy density, ρ_0 is the mass density and C_v is the constant volume [119] specific heat capacity.

[120] **C.   Derivation of initial temperature-pressure initial conditions**

[121] To understand how a temperature increase results in the generation of pressure waves, it [122] is necessary to consider the following two thermodynamic identities [13]:

$$\Delta \rho = \rho_0 K_T \Delta p - \rho_0 \beta \Delta T \tag{3}$$

[123] and

$$v_s^2 = \frac{C_p}{K_T \rho_0 C_v}, \tag{4}$$

[124] where K_T is the isothermal compressibility coefficient, p is the differential pressure, β [125] is the isobaric expansion coefficient, v_s is the speed of sound, and C_p is the specific heat [126] capacity at constant pressure.

[127] Again, it is assumed that heat energy is deposited on a time scale shorter than it takes for [128] the medium density to change, thus $\Delta \rho$ in Eq. 3 is set to zero and the identity is rearranged [129] to yield:

$$\Delta p = \frac{\beta}{K_T} \cdot \Delta T. \tag{5}$$

Inserting Eq. 2 into Eq. 5 yields:

$$\Delta p = \frac{\beta}{K_T \rho_0 C_v} H \tag{6}$$

and combining with Eq. 4 results in:

$$\Delta p = \frac{\beta v_s^2}{C_p} H, \tag{7}$$

which relates the pressure increase to the deposited heat energy through material specific constants. The isobaric expansion coefficient, speed of sound, and specific heat capacity at constant pressure are all properties of the material being irradiated, and combine to form the Grüneisen coefficient, Γ, a dimensionless, material specific constant that indicates the conversion efficiency between the deposited heat energy and pressure variation:

$$\Gamma = \frac{\beta v_s^2}{C_p}. \tag{8}$$

Thus, the initial pressure distribution induced following a pulse of ionizing radiation at a given location, $\mathbf{r}$, can be related to deposited heat energy through:

$$p_0(\mathbf{r}) = \Gamma(\mathbf{r}) \cdot H(\mathbf{r}). \tag{9}$$

Finally, this initial condition can be rewritten in terms of ionizing radiation dose deposited at a given location, $D(\mathbf{r})$, as:

$$p_0(\mathbf{r}) = \Gamma(\mathbf{r}) \cdot D(\mathbf{r}) \cdot \rho(\mathbf{r}) \cdot (1 - k_{HD}(\mathbf{r})). \tag{10}$$

D. Propagation of acoustic pressure waves

The spatially varying differential pressure distribution induced following a pulse of radiation causes the generation of acoustic waves, which propagate provided that the irradiated material is elastic and inertial. This is governed by the thermoacoustic wave equation, which

7

145 describes the evolution and the propagation of the acoustic pressure waves following a pulse
146 of deposited heat energy:

$$\nabla^2 p(\mathbf{r}, t) - \frac{1}{v_s^2} \frac{\partial^2}{\partial t^2} p(\mathbf{r}, t) = -\frac{\beta}{C_p} \frac{\partial}{\partial t} H(\mathbf{r}, t). \tag{11}$$

147 The thermoacoustic wave equation can be solved numerically with a Green's function
148 approach to yield the pressure at a given time, t, and location, $\mathbf{r}$, assuming an impulsive
149 heating source [14]:

$$p_\delta(\mathbf{r}, t) = \frac{1}{4\pi v_s^2} \frac{\partial}{\partial t} \left[\int d\mathbf{r'} \frac{p_0(\mathbf{r'})}{|\mathbf{r} - \mathbf{r'}|} \delta \left(t - \frac{|\mathbf{r} - \mathbf{r'}|}{v_s} \right) \right]. \tag{12}$$

150 Thus far, it has been assumed that heat energy is deposited instantaneously. For this
151 assumption to hold, the heating pulse must satisfy both thermal and stress confinement con-
152 ditions, meaning the pulse of ionizing radiation must be shorter than the thermal relaxation
153 time, τ_{th}, and the stress relaxation time, τ_s:

$$\tau_{th} = \frac{d^2}{\alpha_{th}} \tag{13}$$

$$\tau_s = \frac{d}{v_s} \tag{14}$$

154 where d is the desired spatial resolution and α_{th} is the thermal diffusivity of the material
155 [14]. Considering a desired spatial resolution of 1 mm in water, Eq. 13 indicates that for
156 a thermal diffusivity of water at room temperature of 0.143 mm^2/s the thermal relaxation
157 time is 7 s. As per Eq. 14, assuming a speed of sound in water is 1480 m/s yields a stress
158 relaxation time of 0.68 μs. While the thermal confinement condition is easily satisfied in
159 ionizing radiation-induced acoustics applications, pulse lengths are typically longer than the
160 stress relaxation time. In order to account for the lack of stress confinement, the solution
161 given by Eq. 12 must be convolved with the temporal profile of the heating pulse, $S(t)$ [14]:

$$p(\mathbf{r}, t) = \int_{-\infty}^{+\infty} dt' p_\delta(\mathbf{r}, t - t') S(t'). \tag{15}$$

162 $S(t)$ is dependent on the source of ionizing radiation. In the case of photon beams
163 produced by clinical linear accelerators $S(t)$ is often rectangular in shape [15], while clinical
164 synchrocyclotrons produce proton beams with Gaussian shaped pulses [16], both with full
165 width half maximum lengths on the order of several microseconds.

166 Before moving on, it is worth briefly discussing Eq. 12 in more depth. As is shown in
167 the delta-function term in Eq. 12, time and distance are linked. The pressure wave that
168 reaches point $\mathbf{r}$ at time t originates at a distance $|\mathbf{r} - \mathbf{r'}| = t \cdot v_s$. This distance specifies a
169 sphere centered at the detection point that gets bigger as time increases. The magnitude of
170 pressure waves that reach the detector are related to the initial pressure distribution that
171 intersects with this sphere. Mathematically, due to the delta-function term, the integral
172 reduces to a spherical surface integration of the initial pressure distribution with an inverse
173 distance amplitude scaling, hence the $1/|\mathbf{r}-\mathbf{r'}|$ term. The time derivative can be interpreted
174 in two ways. The pressure waves are shaped by the radial gradient of the spherical surface
175 integration of the initial pressure distribution since the time derivative can be conceptually
176 translated into a spatial derivative due to the time/distance relationship. Due to the prop-
177 erties of convolution, when Eq. 15 is considered the time derivative can instead be applied
178 directly to the temporal profile of the heating pulse, $S(t)$. Thus, the detected pressure waves
179 will be related to the time derivative of the heating pulse. Hence, acoustic emissions are
180 only induced by temporally varying radiation sources.

181 **E. Image reconstruction**

182 The goal of image reconstruction in ionizing radiation-induced acoustics is to reconstruct
183 an image of the initial pressure distribution induced following the pulse of radiation, as given
184 by Eq. 9 and Eq. 10. To reconstruct such an image, pressure signals need to be acquired
185 tomographically, i.e., at multiple angles surrounding the irradiated object. The most basic
186 way of reconstructing the initial pressure distribution is by back-projecting the detected
187 time varying pressure signals, $p(\mathbf{r}, t)$, using the universal back-projection algorithm [17]:

$$p_0(\mathbf{r'}) = \int_S d\Omega_0 p(\mathbf{r}, t) \Bigg|_{v_s t = |\mathbf{r}-\mathbf{r'}|}, \tag{16}$$

188 where Ω_0 refers to the solid angle of the entire detection surface S considering a source

9

point at **r'**. The universal back-projection algorithm has been proven to be exact for spherical, cylindrical and planar detection geometries, however, it is unable to account for irregular geometries or material heterogeneities [18]. It is important to emphasize that unlike traditional computed tomography (CT) back-projection, pressure signals are back-projected on a spherical surface, rather than along a line as in CT, due to the spherical nature of pressure wave propagation. Fig. 2 demonstrates this principle.

Another commonly used algorithm for thermoacoustic reconstruction problems is time reversal, which considers the detected time-varying pressure signals as a pressure source. The algorithm transmits the detected signals back into the medium in time reversed order using numerical methods, such as time domain finite difference [19] and k-space pseudospectral [20, 21] techniques. Time reversal algorithms are valid for any closed geometry and can account for material heterogeneities and signal attenuation [22]. As a result, they are more accurate but more computationally intensive than back-projection based methods.

III. INITIAL IONIZING RADIATION-INDUCED ACOUSTICS STUDIES

A. Early studies

The first reported study to demonstrate the emission of acoustic waves by ionizing radiation was in the particle physics context, where the acoustic waves induced by a 200 MeV proton beam produced by a linear accelerator and a 158 MeV cyclotron beam were detected using a hydrophone in a water tank [23]. This study comprehensively investigated how the detected acoustic signal depended on the proton beam diameter, the amount of energy deposited, the distance between the proton beam and the hydrophone, and the irradiated medium. Their findings were consistent with the thermoacoustic effect, thus other possible mechanisms for the formation of acoustic waves, such as microbubble implosion and molecular dissociation, were ruled out.

The experimental observation of acoustic waves induced by an x-ray beam was first reported in 1983 [24]. Various metals were irradiated by a synchrotron x-ray beam, and the induced acoustic waves were detected by an ultrasound transducer. The thermoacoustic effect was first applied to x-ray dosimetry in 1983 when a cell containing a microphone was constructed to absorb a kV x-ray beam [25]. A linear relationship between the x-ray

10

²¹⁸ beam intensity and the induced acoustic signal was observed, and the authors recognized
²¹⁹ the possibility of expanding this technique to dosimetry measurements of other radiation
²²⁰ beams.

²²¹ Following these initial developments, it was shown that the acoustic waves induced by
²²² clinical therapeutic electron [26], photon [27], and proton [28] beams were detectable in
²²³ water, indicating that acoustic dosimetry techniques could be feasible in a radiotherapy
²²⁴ setting. A breakthrough in the field occurred in 1995 when Hayakawa et al. demonstrated
²²⁵ the detection of acoustic waves *in vivo* during proton therapy treatment of a hepatic patient
²²⁶ [29]. Fig. 1 shows the detected hydrophone signal overlaid on the patient CT scan and
²²⁷ treatment plan. Peaks in the acoustic signal were shown to correspond to dose distribution
²²⁸ gradients and anatomical boundaries. The authors further speculated on the possibility of
²²⁹ using a transducer array surrounding the patient to image the 3D dose distribution, as well
²³⁰ as combining this technique with diagnostic ultrasound to register dosimetric information
²³¹ onto an anatomical image.

²³² **B. Revitalization of the field**

²³³ Despite the promising results in these early studies, very little work was done regarding
²³⁴ the use of ionizing radiation-induced acoustics in medicine until recently. In early 2013,
²³⁵ Xiang et al. proposed x-ray acoustic computed tomography (XACT), an imaging modality
²³⁶ that uses a pulsed x-ray beam to induce acoustic waves [30]. They experimentally demon-
²³⁷ strated the ability to image a lead rod embedded in chicken breast tissue with a clinical
²³⁸ linac photon beam by rotating a transducer around the sample and detecting the induced
²³⁹ pressure waves at 200 positions surrounding the object. Later that year, Stantz et al. pre-
²⁴⁰ sented an abstract demonstrating, through computer simulations, the feasibility of using
²⁴¹ radiation induced-acoustic principles to map three dimensional proton distributions as a
²⁴² method of localizing the Bragg peak [31]. These studies, along with recent advancements in
²⁴³ photoacoustic imaging technologies and the need for volumetric x-ray dosimetry measure-
²⁴⁴ ments and accurate range verification in proton therapy, triggered numerous publications in
²⁴⁵ this field over the past five years. The following sections detail recent studies and provide
²⁴⁶ a future outlook on the potential applications and current challenges of ionizing radiation-
²⁴⁷ induced acoustics in three main areas: linac photon beam dosimetry, proton therapy range

₂₄₈ verification, and medical imaging.

IV. LINAC PHOTON BEAM DOSIMETRY

A. Motivation

₂₅₁ Dosimetry is a crucial part of photon beam radiotherapy to ensure that the delivery ₂₅₂ of radiation to the patient is well characterized and accurately known. Reference or rela- ₂₅₃ tive dosimetry measurements in a phantom are used for beam characterization, treatment ₂₅₄ planning and quality assurance, while *in vivo* dosimetry measurements are made during ₂₅₅ treatment to directly measure the dose received by the patient. Due to the increasing ₂₅₆ complexity of linac treatment delivery techniques, such as intensity modulated radiation ₂₅₇ therapy (IMRT) and volumetric modulated arc therapy (VMAT), there is an increased need ₂₅₈ for volumetric dosimetry techniques to accurately measure the dose delivered to a phantom ₂₅₉ and to verify that treatment delivery matches the planning objectives [6]. Additionally, ₂₆₀ the International Atomic Energy Agency (IAEA) suggests that *in vivo* dosimetry should be ₂₆₁ used for patients that are receiving treatment via novel delivery techniques, after software ₂₆₂ or equipment changes, in hypofractionated treatments, and curative treatments where the ₂₆₃ dose received is potentially close to surrounding normal tissue tolerance [32]. These ad- ₂₆₄ vancements and recommendations have necessitated the development of novel efficient and ₂₆₅ volumetric dosimetry techniques.

₂₆₆ By detecting the acoustic waves induced in an object following irradiation by a linac ₂₆₇ x-ray beam, XACT forms images that can be related to radiation dose. As such, it has long ₂₆₈ been proposed that XACT could be used for a variety of dosimetry applications. After the ₂₆₉ recent initial demonstration of XACT [30], various groups have worked on applying XACT ₂₇₀ to radiotherapy dosimetry applications in two main areas: relative water tank dosimetry ₂₇₁ and *in vivo* dosimetry.

B. Recent work

₂₇₃ Initial studies applying XACT to linac photon beam dosimetry focused on the detec- ₂₇₄ tion of the acoustic waves induced following the irradiation of metal blocks due to the ₂₇₅ high Grüneisen coefficient of metals and, consequently, the resulting large induced acoustic

₂₇₆ signal-to-noise ratio (SNR). The detection of such induced acoustic waves was demonstrated

₂₇₇ using a single element immersion transducer [15, 33], a hydrophone [34], and a commercial

₂₇₈ diagnostic ultrasound transducer [35]. Additionally, the effect of changing different set-up

₂₇₉ parameters and the link between deposited dose and acoustic signal were systematically

₂₈₀ investigated and analyzed [15]. During this time, a comprehensive computer simulation

₂₈₁ workflow combining Monte Carlo dose calculations and acoustic wave transport techniques

₂₈₂ was developed to guide experimental investigations in this area. This simulation tool was

₂₈₃ validated experimentally using simple geometries with metal block measurements [15].

₂₈₄ Later studies investigated using XACT to image dose distributions of various shapes and

₂₈₅ sizes in a homogeneous water tank [36]. Experimental XACT images were obtained by keep-

₂₈₆ ing an immersion transducer stationary while the linac collimator was rotated. Transducer

₂₈₇ signals were acquired every 6° around the radiation field and images were reconstructed

₂₈₈ using a simple back-projection algorithm. Profiles extracted from XACT images were com-

₂₈₉ pared to ion chamber measurements to verify the linear relationship between XACT image

₂₉₀ intensity and delivered radiation dose. Fig. 3 demonstrates the ability of XACT to image

₂₉₁ a puzzle piece shaped field and the agreement between profiles extracted from experimental

₂₉₂ and simulated XACT images and ion chamber measurements. Of note is the negative inten-

₂₉₃ sity ring artifact surrounding the radiation field present in both simulated and experimental

₂₉₄ images, likely due to the limited transducer bandwidth. A subsequent XACT characteri-

₂₉₅ zation study demonstrated that XACT images of acceptable SNR can be formed at a dose

₂₉₆ level as low as 11.6 mGy, and that changes in field size of 4 mm, field location of 2 mm, and

₂₉₇ field magnitude of 3% are detectable with the above implementation of XACT [37]. These

₂₉₈ latest studies demonstrated the viability of using XACT as a relative water tank dosimetry

₂₉₉ technique in a clinical radiotherapy environment.

₃₀₀ The possibility of using XACT for *in vivo* dosimetry has been investigated through sim-

₃₀₁ ulations [38, 39]. In such simulations, the initial pressure distribution following a pulse of

₃₀₂ irradiation was calculated using Monte Carlo dose simulations [7] and Eq. 10. The MAT-

₃₀₃ LAB toolbox k-Wave [21] was then used to model the propagation of the resulting acoustic

₃₀₄ waves and obtain the time-varying pressure signal at the simulated transducer location. The

₃₀₅ first study in this area investigated using a circular array of transducers enclosing the pelvic

₃₀₆ region to reconstruct the dose deposited during a prostate treatment [38]. It was concluded

₃₀₇ based on the amplitude and the frequency of the simulated pressure waves that the induced

13

acoustic signal should be experimentally detectable *in vivo*, however, the need to have an ultrasound transducer array surrounding the patient during treatment could be practically challenging. This led to a study investigating the use of a single transperineal ultrasound transducer to detect the acoustic waves induced during a prostate VMAT treatment [39]. The simulated transducer signal was backprojected onto the patient CT and peaks in the acoustic signal were shown to correspond to gradients in the dose distribution. This principle is demonstrated in Fig. 4, where the detection geometry is shown in Fig. 4a and the dose profile and back-projected acoustic signal along the projection line are displayed in Fig. 4b. Additionally, the ability to detect set-up errors of 3 mm based on the temporal shift of the signal was demonstrated.

C. Future outlook

XACT is a promising technique for water tank dosimetry, and with further developments could be used for routine relative dosimetry measurements such as percent depth dose curves, dose profiles, tissue phantom ratios, and 2D/3D measurements of non-standard radiation fields. Ideally, a commercial XACT system for water tank measurements would consist of a circular transducer array that encloses the radiation field. This would allow for the simultaneous acquisition of signals at different angles surrounding the field, and therefore rapid imaging.

XACT has numerous advantageous characteristics that make it a promising technique for water tank dosimetry applications. There is a linear relationship between deposited dose and induced pressure in a homogeneous medium. Additionally, XACT is dependent on the dose deposited per pulse, meaning it can be considered energy and dose rate independent [37]. Also, XACT does not perturb the radiation beam provided the transducers are placed outside the beam path. These features of XACT simplify calibration and eliminate the need for many of the correction factors required by other dosimetry techniques.

While previous work has been limited to 2D, XACT is inherently 3D due to the spherical propagation of acoustic waves, and 3D images could be reconstructed provided an appropriate transducer acquisition system is used. Initial studies have displayed relative XACT images, however it could be possible to use XACT for absolute dosimetry measurements provided the heat defect, physical density and Grüneisen coefficient are accurately known,

14

₃₃₈ and the transducer and amplification system is well calibrated and characterized.

₃₃₉ An important challenge of translating XACT into a viable clinical water tank dosimetry
₃₄₀ technique is the achievable resolution. Linac pulse envelope lengths typically range from 3
₃₄₁ μs to 4 μs, which roughly translates into an in-water spatial resolution of 4.4 mm to 5.9 mm.
₃₄₂ It is possible to shorten the linac pulse length, but this is typically not done clinically and
₃₄₃ leads to decreased acoustic signal amplitude since less dose is deposited per pulse. Signal
₃₄₄ processing techniques such as deconvolution of the detected transducer signals from the linac
₃₄₅ pulse shape could be an interesting approach to resolve this problem provided the radiation
₃₄₆ pulse structure and signal acquisition system can be properly modelled.

₃₄₇ Another key challenge of XACT is its sensitivity to detecting small amplitude acoustic
₃₄₈ waves. Lower energy beams are typically calibrated to deliver less dose per pulse than the
₃₄₉ higher energy flattening filter free beams used in previous XACT studies [36]. Improvements
₃₅₀ in detection amplification will be necessary to accurately image radiation fields delivered by
₃₅₁ 6 MV photon beams without the need for excessive signal averaging. Additionally, designing
₃₅₂ transducers or hydrophones with an appropriate central frequency and bandwidth for the
₃₅₃ intended application can further improve signal detection sensitivity.

₃₅₄ More sophisticated signal processing and image reconstruction techniques are expected to
₃₅₅ be useful for obtaining higher quality XACT images. Previous studies used a simple back-
₃₅₆ projection algorithm for reconstruction. The resulting XACT images suffered from negative
₃₅₇ intensity ring artifacts, likely primarily caused by the finite bandwidth of the transducer.
₃₅₈ Applying iterative reconstruction algorithms [40], particularly those with non-negative con-
₃₅₉ straints [41], could help solve this problem. The possibility of accounting for signal frequency
₃₆₀ components lost in detection should also be investigated to improve the accuracy of the re-
₃₆₁ constructed images.

₃₆₂ The simulation studies described in section IV B indicate that XACT is a promising *in*
₃₆₃ *vivo* dosimetry technique as well. Since acoustic waves are induced and detected following
₃₆₄ a single pulse of radiation, XACT could provide a near real-time methodology for verifying
₃₆₅ treatment delivery as an alternative to using implanted and invasive dosimeters or relying
₃₆₆ on indirect exit dosimetry techniques [42].

₃₆₇ One of the most promising aspects of using XACT for *in vivo* dosimetry is the potential
₃₆₈ of combining it with anatomical ultrasound imaging. The use of intrafractional ultrasound
₃₆₉ imaging to monitor target motion during treatment is becoming increasingly more com-

15

370 mon [43], and combining intrafractional ultrasound with XACT is an interesting possibility.
371 Theoretically, the same transducer could be used to acquire B-mode anatomical ultrasound
372 images and to detect radiation-induced acoustic signals, allowing the inherent registration
373 of the ultrasound image with dosimetric information. One can imagine a system where the
374 expected acoustic signal based on the patient plan is simulated prior to treatment, and treat-
375 ment is halted if the acoustic signal detected during treatment deviates significantly from
376 what is expected. Combined with ultrasound target tracking, this could allow for real-time
377 verification that dose is being delivered to the desired location in the patient. Additionally,
378 the combination of XACT with anatomical ultrasound could allow for improved accuracy of
379 dosimetric information, since knowledge regarding tissue heterogeneities could be extracted
380 from the anatomical ultrasound image and considered during XACT image reconstruction.

381 Current commercial diagnostic ultrasound transducers will likely not be suitable for com-
382 bined anatomical and dosimetry measurements due to the different frequency requirements
383 of the two modalities. Anatomical imaging requires transducers with a central frequency
384 between 3-10 MHz depending on the site, while the detection of induced acoustic waves is
385 optimal with a wide bandwidth transducer with a central frequency in the hundreds of kHz
386 frequency range. Thus, dual frequency transducers are likely to be required. Such trans-
387 ducers have been developed for ultrasound-guided high intensity focused ultrasound (HIFU)
388 applications, where a low frequency portion of the transducer is used for therapeutic pur-
389 poses and the higher frequency region is used for imaging [44]. Similarly, dual frequency
390 transducers have been developed for contrast enhanced harmonic ultrasound imaging [45].
391 While combined diagnostic ultrasound/XACT imaging will likely require the development of
392 novel transducer technology, the principles behind the dual frequency transducers previously
393 constructed for these other uses could be applicable.

394 Previous simulation studies have assessed the detection of acoustic signals both using an
395 ultrasound array surrounding the patient [38] and using a single transducer [39]. While an
396 array allows for 3D reconstruction of the dose distribution, the placement of transducers in
397 such a geometry may be difficult due to radiation beam interference. However, it could be
398 possible to account for transducers during the treatment planning stage [46], and a recent
399 study demonstrated the construction and operation of a radiolucent transducer [47]. Using
400 a single transducer limits the amount of dosimetric information that can be extracted from
401 detected acoustic signals, however, clinical implementation may become easier.

The integration of XACT into the clinical workflow will be aided by developments in intrafractional ultrasound imaging since many of the challenges arising from placing a transducer in contact with the patient during radiotherapy delivery have already been investigated in the literature. Intrafractional ultrasound imaging has been clinically demonstrated for tracking the target during prostate [48], liver [49] and pancreas [50] treatments. Due to the same requirements for acoustic wave propagation for both XACT and diagnostic ultrasound, XACT is expected to be applicable to the same clinical sites that are accessible by diagnostic ultrasound, namely the breast, liver, kidney, pancreas, prostate, cervix, uterus, bladder and rectum [43].

Finally, it should be noted that while the previous discussion has focused on linac photon beam dosimetry, these concepts are also expected to be extendible to the dosimetry of electron beams produced by clinical linear accelerators.

V. PROTON THERAPY RANGE VERIFICATION

A. Motivation

A major, yet unsolved, issue in proton therapy is the ability to locate the maximum of energy deposition, i.e, the Bragg peak, ideally in real-time and non-invasively during patient treatment. Despite continued advances in the ability of computational models to accurately predict the therapeutic dose to be delivered [51, 52], several sources of uncertainties in the actual delivery remain. These uncertainties are mostly related to the calibration of X-ray CT imaging data into proton stopping power relative to water for treatment planning, in addition to set-up errors and possible anatomical variations during the course of fractionated therapy [53]. Currently, uncertainties in the proton beam range are on the order of 2.5-4.5%. In addition to this range-dependent uncertainty, 1-3 mm are added to range safety margins during treatment planning [53]. There is also careful consideration of beam angles to avoid the placement of the Bragg peak immediately before radiosensitive organs. Although such choices enable a safe delivery of treatment plans under consideration of the above mentioned range uncertainties, they restrict the possibilities of dose escalation due to the non-negligible exposure of healthy tissue, which generally limits full exploitation of the ballistic advantages offered by proton beams.

To this end, detection of secondary emissions for *in vivo* verification of the beam range is a very active area of research worldwide, aiming to reduce the above mentioned range uncertainties for safer delivery of more conformal treatments in the clinical practice. So far most of the studies already reaching clinical testing have been focused on bulky instrumentation aiming to detect primarily photon radiation resulting from nuclear-based interactions, so called positron-emission-tomography and prompt gamma imaging [54, 55].

On the other hand, interest was recently renewed in the exploitation of acoustic emissions, which are intrinsically related to the energy deposition process. In contrast to the already mentioned earlier attempts in the 1990s [29], the trend of modern technologies with superposition of narrow pencil beams (so called pencil beam scanning, [56]), even intrinsically pulsed in the case of latest-generation compact proton therapy accelerators [57], inherently favors generation of acoustic emissions according to Eq. 11 and Eq. 12. Therefore, several groups are currently investigating proton-induced acoustic emissions (so called protoacoustics or, more generally, ionoacoustics) as a promising method to provide *in vivo* and real-time localization of selected pencil beams delivered to the patient, co-registered to tissue anatomy visualized with conventional ultrasound imaging for favorable sites of good sonic accessibility. Owing to the already discussed relationship between energy deposition and acoustic emissions, this method might also open the longer-term perspective of reconstructing the actual dose delivery, at least for selected pencil beams generating sufficient acoustic signals, for novel concepts of adaptive therapy during a treatment course.

B. Recent work

There has been a recent resurgence of interest in thermoacoustic-based proton range verification. Due to the proliferation of proton therapy, expanded access to proton beams, and increased computational power, experimental and simulation work in the field has escalated following a decade-long lull since the 1990s experiments [28, 29].

To understand the potential of the technique, initial simulations focused on feasibility studies and exploring the information content of proton-induced acoustic waves. Alsanea et al. proposed radiation-induced acoustic computed tomography (RACT) in which the proton-induced acoustic signal measured by an array of transducers is used to reconstruct the 3D dose distribution through a filtered backprojection algorithm [31, 58]. The recon-

struction accuracy of clinical pencil beam dose depositions was investigated as a function of noise level and number of projection angles. For low noise levels (approximately equal to the maximum signal pressure amplitude), RACT showed sub-millimeter proton range verification and <2% dosimetric Bragg peak accuracy. Although promising, RACT requires multiple measurements - on the order of 10^3 detection points.

Previous [28, 29] and subsequent studies have focused on range verification using one or a few transducers. Jones et al. simulated a pencil-beam proton dose deposition in a homogeneous water medium, and, consistent with previous experiments [59], showed that it generates two macroscopic waves, labelled "α" and "γ" [60]. The α-wave is generated by the cylindrical pre-Bragg peak portion of the dose deposition, and its arrival time is related to the distance between detector and beam axis. The γ-wave is induced by the Bragg peak, and its arrival time reports on the distance between the detector and the Bragg peak. For detectors placed at a depth greater than the Bragg peak, a single pressure wave (γ) is observed. Simulations confirmed previous intuition [28, 29] and later systematic studies by Albul et al [59], that through time-of-flight calculations the detector-to-Bragg-peak distance may be calculated by multiplying the γ-wave arrival time by the speed of sound in the medium [60]. Further simulation work showed that the central frequency of the proton-induced acoustic spectrum is <400 kHz, and predicted that the acoustic waves induced by a single proton pulse depositing on the order of $10^1 - 10^2$ mGy are detectable by 5 cm diameter transducers even in the presence of thermal noise [61].

As described in Eq. 15, thermoacoustic pressure waves depend on the temporal shape of the excitation pulse. If the pulse is shorter than the acoustic transit time across the Bragg peak's longitudinal dimension then stress confinement is achieved and the acoustic pressure waves are dictated by the spatial shape of the dose deposition. If the pulse is longer, stress confinement is not achieved and the acoustic waves are affected. Simulations examining the effect of proton pulse lengths concluded that the ideal proton pulse length and shape are on the cusp of stress confinement [62]. For clinical proton beams, Gaussian proton pulses with a full-width half-maximum (FWHM) of roughly 5 μs are expected to generate acoustic waves with the highest SNR per deposited dose assuming the acoustic signal is averaged over multiple proton pulse deliveries. The studies also found that SNR is maximized by increasing the instantaneous proton pulse intensity.

Recently, clinical experiments have been challenged by producing proton pulses with en-

19

velopes that are short enough to generate a detectable acoustic signal. Clinically common proton sources (cyclotron and synchrotron) deliver millisecond-to-second long macrostructure proton pulses [63]. Unlike joint clinical/research centers, which have the ability to dispense individual 50 ns synchrotron bunches separated by 50 ms periods [28], clinical proton pulses consist of 0.5-50 ns microstructure bunches delivered at >5 MHz repetition rates [55]. Because this <200 ns repetition period is much smaller than the stress confinement criteria, the microstructure is undetectable in the acoustic signal and the pressure emissions are shaped by the macrostructure proton pulse envelope. The newest clinical sources, synchrocyclotrons, clinically deliver approximately 3.5 μs FWHM Gaussian proton pulses [16], which are predicted to be ideal for acoustic wave generation [62]. To experimentally characterize proton-induced thermoacoustics, researchers have first used accessible non-clinical proton sources [64, 65], and modified others [66]. To generate detectable acoustic signals using a clinical IBA 230 cyclotron, Jones *et al.* modified the proton pulse output by modulating the proton current entering the cyclotron with a function generator [66]. With this method, they were able to generate approximately Gaussian proton pulses of roughly 17 μs FWHM, and the arrival times of the hydrophone-detected pressure waves were proportional to detector distance from the beam. Significant averaging was required due to noise. Other experiments using the same cyclotron modulation method (and the same 17 μs, non-ideal proton pulses) projected a precision in arrival time measurement of 2.2 mm (standard deviation) based on averaging signals induced by 2 Gy (at high currents of 10^8 protons per pulse) of deposited dose [67]. More recently, experiments in a water phantom were performed at the world's first clinical synchrocyclotron at the Centre Antoine-Lacassagne (CAL, Nice, France) [16], which delivered a pencil beam in proton pulses of about 3 μs pulse width and 1 kHz repetition rate, therefore ideal conditions for ionoacoustic range measurements not needing any further beam modifications. Using a hydrophone in axial geometry distal to the beam stopping point along with a trigger from a scintillator-based detector, the Bragg peak position could be measured with an accuracy and precision of better than 1 mm compared to Stringray ionization chamber based range measurements as well as Geant4 simulations, as seen in Fig. 5. However, 1000 fold averaging was necessary to obtain sufficient SNR, resulting in a Bragg peak dose of about 10 Gy. Nevertheless, all authors of the above mentioned studies identified future possibilities of signal enhancement when using multiple, and more sensitive detectors.

The proton-induced acoustic waves are bipolar. A positive compression peak reaches the detector first and is followed by a negative rarefaction peak. For non-RACT methods that seek to determine the proton range based on a time-of-flight calculation (protoacoustics/ionoacoustics), the distance between detector and Bragg peak is calculated by multiplying the acoustic arrival time by the speed of sound in the medium. This raises the question of where to measure the arrival time. A number of methods have been used, including measuring the arrival time from the compression peak [64], the midpoint between compression peak and rarefaction trough [60], deconvolving the proton pulse [67], and measuring from the earliest appearance of the pressure wave [68]. By projecting the cumulatively-integrated pressure waves measured at a few detectors, a beam-forming reconstruction has also been used [69]. Although the Bragg peak distance is close to that predicted by the zero cross-over point between compression and rarefaction peaks, there is no universally correct arrival time definition; the Bragg peak asymmetry imprints itself on the acoustic wave in a complicated way that depends on detector position [62]. Depending on the used arrival time definition, an offset might be required [64]. There is also ambiguity in the detector response that may introduce a delay that must be calibrated to accurately convert arrival time into distance [16, 67].

An additional intriguing feature of acoustic-based range verification is its possible combination with ultrasonic visualization of tissue anatomy, as discussed earlier with XACT for linac photon beam dosimetry. To this end, ionoacoustic measurements of the proton Bragg peak in combination with ultrasound and optoacoustic imaging was reported for the first time in an *ex vivo* mouse experiment at a non-clinical low-energy (approximately 20 MeV) pulsed proton source, as seen in Fig. 6 [70]. In the same year, Patch et al. performed intrinsically co-registered ionoacoustic and ultrasonic acquisitions of water and a gelatine phantom by another specially manipulated non-clinical low-energy (50 MeV) proton source using a cardiac ultrasound transducer array [65]. This measurement required a signal integration of 1024 pulses corresponding to over 2000 Gy of total dose delivery. For clinical proton energies, dedicated devices will need to be developed in order to provide the required frequency spectra for ultrasound imaging (MHz) and proto/ionoacoustic sensing (kHz), ideally integrated in a single system for intrinsic co-registration. Such an advanced technology could enable near real-time visualization of the Bragg peak position superimposed on the tissue anatomy for verification of the beam delivery on a spot-by-spot basis, ideally enabling

557 image guided compensation of tumour motion.

558 All of the recent work described above, with the notable exception of [70], has been per-
559 formed in homogeneous materials, almost exclusively water. Translating the acoustic-based
560 proton range verification technique from water to heterogeneous tissue presents a number
561 of challenges. The tissue heterogeneity manifests itself in two ways: (i) the initial pressure
562 distribution will vary with the Grüneisen coefficient (Eq. 8) of the underlying tissue, and
563 (ii) the acoustic wave propagation will be affected by the tissue-dependent speed of sound,
564 attenuation, and reflection. Of these, the speed of sound dependence appears to be the most
565 challenging hurdle for accurate range verification because the time-of-flight calculation re-
566 quires knowledge of the speed of sound. To understand the effects of heterogeneity, CT-based
567 k-Wave simulations have been performed that assign the Grüneisen coefficient and speed of
568 sound to each voxel based on the tissue type, as determined by Hounsfield Unit value [69, 71].
569 Simulations by Patch et al. predict that accurate range verification is achievable during a
570 clinical prostate treatment using a transrectal probe. By comparing the measured acoustic
571 wave arrival times to a pre-calculated simulated dataset, local heterogeneity-induced varia-
572 tions could be corrected to give <2 mm errors in range calculation accuracy [69]. Another
573 set of simulations compared the acoustic propagation of the same initial pressure distribu-
574 tion over homogeneous water and heterogeneous liver and prostate sites, as shown in Fig. 7
575 [71]. For the considered liver case, tissue attenuation was only about 1 dB, and the average
576 speed of sound between detectors and the Bragg peak differed by $\leq 2.2\%$ compared to the
577 speed of sound in water. For the few considered prostate beams, short proton pulses may
578 allow for proton range verification with an accuracy of <2 mm if the detectors are placed
579 distal to the Bragg peak and the beam propagation axis is known a priori [71].

580 **C. Future outlook**

581 The promising results reported by several groups encourage the ongoing efforts to over-
582 come one of the major remaining challenges of ionoacoustic range verification, namely im-
583 proving the SNR for monitoring individual pencil beams at typical therapeutic doses. Along
584 with possibilities of signal enhancement at the clinical proton sources with proper beam
585 pulsing and elevated instantaneous dose rate, detector technologies can also be advanced
586 to enable utmost sensitivity in the relatively low frequency range (10-100 kHz) of proton-

22

induced acoustic emissions, ideally in combination with ultrasound imaging. Moreover, utilization of multiple detectors - as already envisioned in the seminal Hayakawa et al paper [29] - can offer an elegant means to overcome the issue of local heterogeneities. Although no multi-element, low frequency arrays have yet been used in the context of acoustic-based proton range verification, triangulation with as few as 3-5 detectors [69, 72] is expected to improve SNR and minimize errors introduced by heterogeneous tissue [71].

Future conceivable clinical workflows could enable verification of the entire delivery for intrinsically pulsed clinical synchrocyclotrons, or pre-treatment range verification of a few "diagnostic spots" [64, 66] from artificially pulsed beams of conventional synchrotrons or cyclotrons. Along with the already discussed integration of ultrasound imaging, proto/ionoacoustic sensing could thus offer a unique, compact and cost-effective means for real-time range verification, and ideally even dose reconstruction of modern proton treatments, with co-registered anatomical confirmation. This could be especially beneficial for those critical tumour indications which are currently challenged by intrafractional organ motion, such as prostate, breast, liver and pancreas [64], thus promising an important step forward in treatment quality and likely long-term outcomes.

VI. MEDICAL IMAGING

A. Motivation

Since Wilhelm Conrad Roentgen discovered the X-ray more than one hundred years ago, X-ray imaging has been an invaluable tool in medical diagnosis, biology, and materials science [73–82]. In particular, X-ray computed tomography (CT) has proven tremendously useful for non-invasive medical imaging since its inception nearly 50 years ago [83]. However, CT requires a large set of projection data and high radiation dose to achieve sufficient image quality. It is estimated that up to 2% of cancer cases are the result of the radiation obtained from CT imaging [84, 85], thus this risk potentially negates many of benefits. XACT takes advantage of high sensitivity to X-ray absorption and high ultrasonic resolution in a single modality [86]. A single projection X-ray exposure is sufficient to generate acoustic signals in 3D space since the X-ray generated acoustic waves are of a spherical nature and propagate in all directions from their point of generation. While CT relies upon a rotating X-ray source

₆₁₆ and many X-ray projections to obtain a 3D image, XACT can generate a 3D image through
₆₁₇ a single X-ray projection, drastically decreasing radiation dose.

₆₁₈ It should be noted that unlike the XACT applications described in section IV, which use
₆₁₉ the acoustic emissions induced by therapeutic megavoltage x-ray beams to reconstruct the
₆₂₀ deposited dose, in the medical imaging application described here a diagnostic X-ray expo-
₆₂₁ sure is used to image the underlying structure based on contrast originating predominantly
₆₂₂ from differential photoelectric effect cross sections and underlying Grüneisen coefficients.

B. Recent work

₆₂₄ XACT imaging as a novel biomedical imaging modality was first proposed and demon-
₆₂₅ strated in 2013 [30], and has since been studied by different groups all over the world in
₆₂₆ various applications [33, 35, 36, 38]. Initially, systems with a single low central frequency
₆₂₇ ultrasound transducer were used for X-ray-induced acoustic signal collection in XACT imag-
₆₂₈ ing studies. A typical XACT imaging system with a single ultrasound transducer requires
₆₂₉ mechanical scanning for acquisition of a two-dimensional (2D) image, requiring multiple
₆₃₀ X-ray pulses and leading to long scan times [30, 36, 86].

₆₃₁ Recently, a new XACT imaging system that yields rapid and high resolution two dimen-
₆₃₂ sional images was developed and tested. A schematic of this system is shown in Fig. 8 [87].
₆₃₃ In this system, a sample is irradiated by a nanosecond-pulsed X-ray source, leading to the
₆₃₄ isotropic emission of acoustic waves. Instead of using a single transducer for detection, a
₆₃₅ ring array of piezoelectric ultrasound transducers detects the acoustic waves and converts
₆₃₆ them to electrical signals. The resulting signals are then back-projected to reconstruct the
₆₃₇ image. It should be noted that as this current system is using a ring-array of transducers,
₆₃₈ only a single 2D slice of the sample can be obtained. 3D imaging would be possible with a
₆₃₉ spherical or cup-shaped array.

₆₄₀ Fig. 9 highlights key results from recent XACT studies. Fig. 9a displays the XACT
₆₄₁ image of 150 μm thick gold fiducial markers acquired using a 60 ns x-ray source and single
₆₄₂ 2.25 MHz transducer. The image was shown to be in good agreement with the corresponding
₆₄₃ CT image, and based on the size of the reconstructed gold fiducial markers XACT spatial
₆₄₄ resolution was determined to be 350 μm [86]. Fig. 9b shows an XACT image of lead sheets
₆₄₅ with thickness 150 μm shaped into the OU logo obtained using the fast XACT imaging

24

₆₄₆ system with the 5 MHz transducer array. This experiment resulted in a spatial resolution ₆₄₇ of 138 μm [87].

C. Future outlook

₆₄₉ Challenges encountered during these experiments were primarily due to equipment lim- ₆₅₀ itations. The images in Fig. 9 required a large number of X-ray pulses to obtain sufficient ₆₅₁ SNR. This large number of pulses can be reduced by two methods, both of which, at the ₆₅₂ time of writing, are being investigated. The first is to increase the amplification of each ₆₅₃ transducer in the ring array, as they are currently amplified at only 52 dB. An amplifier ₆₅₄ with enough channels to match each transducer element on the ring-array is necessary to do ₆₅₅ this. Second, the fluence of the X-ray tube can be increased with new X-ray sources, such ₆₅₆ as the laser-driven Thomson X-ray source [88, 89].

₆₅₇ It is believed that XACT imaging will find broad applications in both basic research and ₆₅₈ clinical care. Considering the use of XACT in breast imaging, minimal X-ray exposure can ₆₅₉ generate a 3D acoustic image of the breast [90], which dramatically reduces the radiation ₆₆₀ dose to patients when compared to conventional breast CT. Bone mineral density mapping ₆₆₁ could also be another possible application for XACT.

VII. CONCLUSIONS

₆₆₃ Based on the promising studies summarized in this article, ionizing radiation-induced ₆₆₄ acoustics based technologies have the potential to be highly useful, real-time, and cost- ₆₆₅ effective tools in three distinct applications. First, XACT could be a powerful tool for ₆₆₆ both relative and *in vivo* linac photon beam dosimetry, with the potential for development ₆₆₇ of a system combining XACT and anatomical ultrasound to visualize the delivered dose ₆₆₈ distribution in near real-time. Secondly, protoacoustics/ionoacoustics is a promising tool to ₆₆₉ accurately localize the Bragg peak and provide range verification for particle therapy, again ₆₇₀ with the potential to be combined with anatomical ultrasound to overlay the position of ₆₇₁ the Bragg peak on patient anatomy during treatment. Thirdly and finally, XACT has the ₆₇₂ potential to be an effective low dose diagnostic imaging modality for sites such as breast ₆₇₃ cancer.

Various technological advances are still required to bring these technologies to the clinic. Studies in all three areas reported a need for the development of novel transducer technologies. In the case of linac photon beam dosimetry and proton therapy range verification applications, novel low frequency transducers with a wide bandwidth are required. Ideally, dual frequency transducers need to be developed to enable the combination of induced acoustic wave detection and anatomical ultrasound imaging. Noise is a current limitation in all three areas, thus the development of highly sensitive transducers in the appropriate frequency range will be required for accurate signal detection at clinically relevant dose levels. Additionally, beam delivery technology optimization will aid in the development of ionizing radiation-induced acoustics techniques. This may take the form of exploiting emerging radiation delivery devices, such as laser driven x-ray sources for medical imaging and synchrocyclotrons for Bragg peak localization, or adapting current radiation delivery technologies, such as decreasing the pulse length of therapeutic linacs or introducing a pulsed beam structure into clinical cyclotrons and synchrotrons used for proton beam therapy.

With the appropriate technological advances and further work investigating how these promising initial studies can be translated into the clinical setting, ionizing radiation-induced acoustics based techniques are expected to have a significant clinical impact to guide cancer treatment delivery and imaging in the near future.

VIII.   ACKNOWLEDGEMENTS

IX.   CONFLICT OF INTEREST

The authors have no conflicts to disclose.

---

[1] A. G. Bell, "On the production and reproduction of sound by light," *American Journal of Science*, vol. 20, no. 118, pp. 305–324, 1880.

26

[2] T. Bowen, "Radiation-induced thermoacoustic soft tissue imaging," in *IEEE Ultrasonics Symposium Proceedings*, pp. 817–822, 1981.

[3] L. Wang and S. Hu, "Photoacoustic tomography: In vivo imaging from organelles to organs," *Science*, vol. 335, no. 6075, pp. 1458–1462, 2012.

[4] S. Zackrisson, S. M. W. Y. van de Ven, and S. S. Gambhir, "Light in and sound out: emerging translational strategies for photoacoustic imaging.," *Cancer Research*, vol. 74, no. 4, pp. 979–1004, 2014.

[5] F. Gao, X. Feng, and Y. Zheng, "Advanced photoacoustic and thermoacoustic sensing and imaging beyond pulsed absorption contrast," *Journal of Optics*, vol. 18, no. 7, 2016.

[6] T. Kron, J. Lehmann, and P. B. Greer, "Dosimetry of ionising radiation in modern radiation oncology," *Physics in Medicine and Biology*, vol. 61, pp. R167–R205, 2016.

[7] I. Kawrakow, "Accurate condensed history Monte Carlo simulation of electron transport. I. EGSnrc, the new EGS4 version," *Medical Physics*, vol. 27, no. 3, pp. 485–498, 2000.

[8] S. Agostinelli, J. Allison, K. Amako, J. Apostolakis, H. Araujo, P. Arce, M. Asai, D. Axen, S. Banerjee, G. Barrand, F. Behner, L. Bellagamba, J. Boudreau, L. Broglia, and A. Brunengo, "GEANT4- A simulation toolkit," *Nuclear Instruments and Methods in Physics Research A*, vol. 506, pp. 250–303, 2003.

[9] R. Forster and T. Godfrey, "MCNP- a general Monte Carlo code for neutron and photon transport," *Monte Carlo Methods and Applications*, vol. 240, pp. 33–55, 1985.

[10] A. Ferrari, P. R. Sala, A. Fasso, and J. Ranft, "FLUKA: a multi-particle transport code," Tech. Rep. CERN-2005-10, Geneva, 2005.

[11] J. Baro, J. Sempau, J. Fernandez-Varea, and F. Salvat, "PENELOPE: An algorithm for Monte Carlo simulation of the penetration and energy loss of electrons and positrons in matter," *Nuclear Instruments and Methods in Physics Research B*, vol. 100, pp. 31–46, 1995.

[12] C. K. Ross, N. V. Klassen, K. Shortt, and G. Smith, "A direct comparison of water calorimetry and Fricke dosimetry," *Physics in Medicine & Biology*, vol. 34, no. 1, pp. 23–42, 1989.

[13] B. T. Cox, J. G. Laufer, and P. C. Beard, "The challenges for quantitative photoacoustic imaging," *Proceedings of SPIE*, vol. 7177, pp. 717713–717713–9, 2009.

[14] Y. Zhou, J. Yao, and L. V. Wang, "Tutorial on photoacoustic tomography," *Journal of Biomedical Optics*, vol. 21, no. 6, p. 061007, 2016.

[15] S. Hickling, P. Leger, and I. El Naqa, "On the detectability of acoustic waves induced following irradiation by a radiotherapy linear accelerator," *IEEE Transactions on Ultrasonics, Ferroelectrics, and Frequency Control*, vol. 63, no. 5, pp. 683–690, 2016.

[16] S. Lehrack, W. Assmann, D. Bertrand, S. Henrotin, J. Herault, V. Heymans, F. Vander Stappen, P. Thirolf, M. Vidal, J. Van de Walle, and K. Parodi, "Submillimeter ionoacoustic range determination for protons in water at a clinical synchrocyclotron," *Physics in Medicine & Biology*, vol. 62, pp. 19–30, 2017.

[17] R. Kruger, P. Liu, Y. Fang, and C. Appledorn, "Photoacoustic ultrasound (PAUS)- Reconstruction tomography," *Medical Physics*, vol. 22, no. 10, pp. 1605–1609, 1995.

[18] M. Xu and L. Wang, "Universal back-projection algorithm for photoacoustic computed tomography," *Physical Review E*, vol. 71, no. 1, p. 016706, 2005.

[19] D.-H. Huang, C.-K. Liao, C.-W. Wei, and P.-C. Li, "Simulations of optoacoustic wave propagation in light-absorbing media using a finite-difference time-domain method," *The Journal of the Acoustical Society of America*, vol. 117, no. 5, pp. 2795–2801, 2005.

[20] T. D. Mast, L. P. Souriau, D. L. Liu, M. Tabei, A. I. Nachman, and R. C. Waag, "A k-space method for large-scale models of wave propagation in tissue," *IEEE Transactions on Ultrasonics, Ferroelectrics, and Frequency Control*, vol. 48, no. 2, pp. 341–54, 2001.

[21] B. E. Treeby and B. T. Cox, "k-Wave: MATLAB toolbox for the simulation and reconstruction of photoacoustic wave fields," *Journal of Biomedical Optics*, vol. 15, no. 2, p. 021314, 2010.

[22] B. E. Treeby and B. T. Cox, "Modeling power law absorption and dispersion for acoustic propagation using the fractional Laplacian," *Journal of the Acoustical Society of America*, vol. 127, no. 5, pp. 2741–48, 2010.

[23] L. Sulak, T. Armstrong, H. Baranger, M. Bregman, M. Levi, D. Mael, J. Strait, T. Bowen, A. E. Pifer, P. A. Polakos, H. Bradner, A. Parvulescu, W. V. Jones, B. Rouge, and J. Learned, "Experimental studies of the acoustic signature of proton beams traversing fluid media," *Nuclear Instruments and Methods*, vol. 161, pp. 203–217, 1979.

[24] W. Sachse, "Observation of x-ray generated ultrasound," in *IEEE Ultrasonics Symposium Proceedings*, pp. 677–680, 1983.

[25] S. Mascarenhas, "A photoacoustical radiation dosimeter," *Medical Physics*, vol. 11, no. 1, pp. 73–74, 1984.

28

[26] T. Bowen, W. G. Connor, R. L. Nasoni, A. E. Pifer, R. Bell, D. H. Cooper, and G. H. Sembroski, "Observation of acoustic signals from a phantom in an 18 MeV electron beam for cancer therapy," in *Acoustical Imaging*, pp. 429–434, New York: Plenum Press, 1984.

[27] T. Bowen, C. X. Chen, S. C. Liew, W. R. Lutz, and R. L. Nasoni, "Observation of ultrasonic emission from edges of therapeutic x-ray beams," *Physics in Medicine and Biology*, vol. 36, no. 4, pp. 537–9, 1991.

[28] J. Tada, Y. Hayakawa, K. Hosono, and T. Inada, "Time resolved properties of acoustic pulses generated in water and in soft tissue by pulsed proton beam irradiation–a possibility of doses distribution monitoring in proton radiation therapy.," *Medical Physics*, vol. 18, no. 6, pp. 1100–1104, 1991.

[29] Y. Hayakawa, J. Tada, N. Arai, K. Hosono, M. Sato, T. Wagai, H. Tsuji, and H. Tsuji, "Acoustic pulse generated in a patient during treatment by pulsed proton radiation beam," *Radiation Oncology Investigations*, vol. 3, pp. 42–45, 1995.

[30] L. Xiang, B. Han, C. Carpenter, G. Pratx, Y. Kuang, and L. Xing, "X-ray acoustic computed tomography with pulsed x-ray beam from a medical linear accelerator," *Medical Physics*, vol. 40, no. 1, p. 010701, 2013.

[31] K. Stantz, F. Alsanea, and V. Moskvin, "Use of radiation-induced ultrasound to image proton dosimetry," *Medical Physics*, vol. 40, no. 6, p. 546, 2013.

[32] International Atomic Energy Agency, "Development of procedures for in vivo dosimetry in radiotherapy," *IAEA Human Health Reports*, vol. 8, 2013.

[33] J. Kim, E.-Y. Park, Y. Jung, B. C. Kim, J. H. Kim, C.-Y. Yi, I. J. Kim, and C. Kim, "X-ray acoustic-based dosimetry using a focused ultrasound transducer and a medical linear accelerator," *IEEE Transactions on Radiation and Plasma Medical Sciences*, vol. 1, no. 6, pp. 534–540, 2017.

[34] X. Diao, J. Zhu, W. Li, N. Deng, C. T. Chin, X. Zheng, X. Zhang, X. Chen, X. Li, and Y. Kuang, "Broadband detection of dynamic acoustic emission process induced by 6 MV therapeutic x-ray beam from a clinical linear accelerator," in *IEEE International Ultrasonics Symposium Proceedings*, pp. 1–4, 2015.

[35] D. R. T. Sampaio, J. H. Uliana, A. O. Antonio, J. F. Pavoni, and T. Z. Pavan, "X-ray acoustic imaging for external beam radiation therapy dosimetry using a commercial ultrasound scanner," in *IEEE International Ultrasonics Symposium Proceedings*, pp. 1–4, 2015.

[36] S. Hickling, H. Lei, M. Hobson, P. Leger, X. Wang, and I. El Naqa, "Experimental evaluation of x-ray acoustic computed tomography for radiotherapy dosimetry applications," *Medical Physics*, vol. 44, no. 2, pp. 608–617, 2017.

[37] S. Hickling, M. Hobson, and I. El Naqa, "Characterization of x-ray acoustic computed tomography for applications in radiotherapy dosimetry," *IEEE Transactions on Radiation and Plasma Medical Sciences*, vol. pp, no. 99, 2018.

[38] S. Hickling, M. Hobson, and I. El Naqa, "Feasibility of x-ray acoustic computed tomography as a tool for noninvasive volumetric in vivo dosimetry," *International Journal of Radiation Oncology Biology Physics*, vol. 90, no. 1, p. S843, 2014.

[39] S. Hickling, M. Hobson, M. Renaud, and I. El Naqa, "In vivo detection of radiation-induced acoustic waves for treatment delivery verification: A simulation study," *Medical Physics*, vol. 44, no. 6, p. 2760, 2017.

[40] G. Paltauf, J. A. Viator, S. A. Prahl, and S. L. Jacques, "Iterative reconstruction algorithm for optoacoustic imaging.," *J. Acoust. Soc. Amer.*, vol. 112, no. 4, pp. 1536–1544, 2002.

[41] L. Ding, X. L. Deán-Ben, C. Lutzweiler, D. Razansky, and V. Ntziachristos, "Image reconstruction in cross-sectional optoacoustic tomography based on non-negative constrained model-based inversion," in *Proceedings of SPIE*, vol. 9539, pp. 953919–4, 2015.

[42] B. Mijnheer, S. Beddar, J. Izewska, and C. Reft, "In vivo dosimetry in external beam radiotherapy," *Medical Physics*, vol. 40, no. 7, p. 070903, 2013.

[43] T. O'Shea, J. Bamber, D. Fontanarosa, S. van der Meer, F. Verhaegen, and E. Harris, "Review of ultrasound image guidance in external beam radiotherapy part II: intra-fraction motion management and novel applications," *Physics in Medicine and Biology*, vol. 61, no. 8, pp. R90–R137, 2016.

[44] T. Azuma, M. Ogihara, J. Kubota, A. Sasaki, S. I. Umemura, and H. Furuhata, "Dual-frequency ultrasound imaging and therapeutic bilaminar array using frequency selective isolation layer," *IEEE Transactions on Ultrasonics, Ferroelectrics, and Frequency Control*, vol. 57, no. 5, pp. 1211–1224, 2010.

[45] K. Martin, B. Lindsey, J. Ma, M. Lee, S. Li, F. Foster, X. Jiang, and P. Dayton, "Dual-frequency piezoelectric transducers for contrast enhanced ultrasound imaging," *Sensors*, vol. 14, no. 11, pp. 20825–20842, 2014.

[46] M. Bazalova-Carter, J. Schlosser, J. Chen, and D. Hristov, "Monte Carlo modeling of ultrasound probes for image guided radiotherapy," *Medical Physics*, vol. 42, no. 10, pp. 5745–5756, 2015.

[47] J. Schlosser and D. Hristov, "Radiolucent 4D ultrasound imaging: system design and application to radiotherapy guidance," *IEEE Transactions on Medical Imaging*, vol. 35, no. 10, pp. 2292–2300, 2016.

[48] A. Trivedi, T. Ashikaga, D. Hard, J. Archambault, M. Lachaine, D. T. Cooper, and H. J. Wallace, "Development of 3-dimensional transperineal ultrasound for image guided radiation therapy of the prostate: Early evaluations of feasibility and use for inter- and intrafractional prostate localization," *Practical Radiation Oncology*, 2016.

[49] J. Schlosser, R. H. Gong, R. Bruder, A. Schweikard, S. Jang, J. Henrie, A. Kamaya, A. Koong, D. T. Chang, and D. Hristov, "Robotic intrafractional US guidance for liver SABR: System design, beam avoidance, and clinical imaging," *Medical Physics*, vol. 43, no. 11, pp. 5951–5963, 2016.

[50] E. A. Omari, B. Erickson, C. Ehlers, F. Quiroz, G. Noid, D. T. Cooper, M. Lachaine, and X. A. Li, "Preliminary results on the feasibility of using ultrasound to monitor intrafractional motion during radiation therapy for pancreatic cancer," *Medical Physics*, vol. 43, no. 9, pp. 5252–5260, 2016.

[51] J. Bauer, F. Sommerer, A. Mairani, D. Unholtz, R. Farook, J. Handrack, K. Frey, T. Marcelos, T. Tessonnier, S. Ecker, B. Ackermann, M. Ellerbrock, J. Debus, and K. Parodi, "Integration and evaluation of automated Monte Carlo simulations in the clinical practice of scanned proton and carbon ion beam therapy," *Physics in Medicine & Biology*, vol. 59, no. 16, pp. 4635–4659, 2014.

[52] J. M. Verburg, C. Grassberger, S. Dowdell, J. Schuemann, J. Seco, and H. Paganetti, "Automated Monte Carlo simulation of proton therapy treatment plans," *Technology in Cancer Research & Treatment*, vol. 15, no. 6, pp. NP35–NP46, 2016.

[53] H. Paganetti, "Range uncertainties in proton therapy and the role of Monte Carlo simulations," *Physics in Medicine & Biology*, vol. 57, no. 11, pp. 99–117, 2012.

[54] K. Parodi, "Vision 20/20: Positron emission tomography in radiation therapy planning, delivery, and monitoring," *Medical Physics*, vol. 42, no. 12, pp. 7153–7168, 2015.

[55] J. Krimmer, D. Dauvergne, J. M. Létang, and É. Testa, "Prompt-gamma monitoring in hadrontherapy: A review," *Nuclear Instruments and Methods in Physics Research Section A: Accelerators, Spectrometers, Detectors and Associated Equipment*, vol. 878, pp. 58–73, 2018.

[56] E. Pedroni, R. Bacher, H. Blattmann, T. Böhringer, A. Coray, A. Lomax, S. Lin, G. Munkel, S. Scheib, U. Schneider, and A. Tourovsky, "The 200-MeV proton therapy project at the Paul Scherrer Institute: Conceptual design and practical realization," *Medical Physics*, vol. 22, no. 1, pp. 37–53, 1995.

[57] S. Henrotin, M. Abs, E. Forton, Y. Jongen, W. Kleeven, J. V. D. Walle, and P. Verbruggen, "Commissioning and Testing of the First Iba S2C2," in *Proceedings of Cyclotrons2016*, pp. 178–180, 2016.

[58] F. Alsanea, V. Moskvin, and K. M. Stantz, "Feasibility of RACT for 3D dose measurement and range verification in a water phantom," *Medical Physics*, vol. 42, no. 2, pp. 937–946, 2015.

[59] V. I. Albul, V. B. Bychkov, S. Vasil'ev, K. Gusev, V. Demidov, E. Demidova, N. Krasnov, A. Kurchanov, V. Luk'yashin, and A. Sokolov, "Acoustic field generated by a beam of protons stopping in a water medium," *Acoustical Physics*, vol. 51, no. 1, pp. 33–37, 2005.

[60] K. C. Jones, A. Witztum, C. M. Sehgal, and S. Avery, "Proton beam characterization by proton-induced acoustic emission: simulation studies," *Physics in Medicine and Biology*, vol. 59, no. 21, pp. 6549–63, 2014.

[61] M. Ahmad, L. Xiang, S. Yousefi, and L. Xing, "Detection threshold of proton-acoustic range verification," *Medical Physics*, vol. 42, no. 10, pp. 5735–5744, 2015.

[62] K. C. Jones, C. M. Seghal, and S. Avery, "How proton pulse characteristics influence protoacoustic determination of proton- beam range: simulation studies," *Physics in Medicine & Biology*, vol. 61, pp. 2213–2242, 2016.

[63] International Commission on Radiation Units and Measurements, "Prescribing, recording, and reporting proton-beam therapy (ICRU Report 78)," tech. rep., ICRU, Bethesda, 2007.

[64] W. Assmann, S. Kellnberger, S. Reinhardt, S. Lehrack, A. Edlich, P. G. Thirolf, M. Moser, G. Dollinger, M. Omar, V. Ntziachristos, and K. Parodi, "Ionoacoustic characterization of the proton Bragg peak with submillimeter accuracy," *Medical Physics*, vol. 42, no. 2, pp. 567–574, 2015.

[65] S. K. Patch, M. Kireeff Covo, A. Jackson, Y. M. Qadadha, K. S. Campbell, R. A. Albright, P. Bloemhard, A. P. Donoghue, C. R. Siero, T. L. Gimpel, S. M. Small, B. F. Ninemire, M. B. Johnson, and L. Phair, "Thermoacoustic range verification using a clinical ultrasound array provides perfectly co-registered overlay of the Bragg peak onto an ultrasound image," *Physics in Medicine and Biology*, vol. 61, no. 15, pp. 5621–5638, 2016.

[66] K. C. Jones, F. V. Stappen, C. R. Bawiec, G. Janssens, P. A. Lewin, D. Prieels, T. D. Solberg, C. M. Sehgal, and S. Avery, "Experimental observation of acoustic emissions generated by a pulsed proton beam from a hospital-based clinical cyclotron," *Medical Physics*, vol. 42, no. 12, pp. 7090–7097, 2015.

[67] K. C. Jones, F. Vander Stappen, C. M. Sehgal, and S. Avery, "Acoustic time-of-flight for proton range verification in water," *Medical Physics*, vol. 43, no. 9, pp. 5213–5224, 2016.

[68] W. Nie, K. C. Jones, S. Petro, A. Kassaee, C. M. Sehgal, and S. Avery, "Proton range verification in homogeneous materials through acoustic measurements," *Physics in Medicine & Biology*, vol. 63, no. 2, p. 025036, 2018.

[69] S. K. Patch, D. E. M. Hoff, T. B. Webb, L. G. Sobotka, and T. Zhao, "Two-stage ionoacoustic range verification leveraging Monte Carlo and acoustic simulations to stably account for tissue inhomogeneity and accelerator-specific time structure - a simulation study," *Medical Physics*, vol. 45, no. 2, pp. 783–793, 2017.

[70] S. Kellnberger, W. Assmann, S. Lehrack, S. Reinhardt, P. Thirolf, D. Queirós, G. Sergiadis, G. Dollinger, K. Parodi, and V. Ntziachristos, "Ionoacoustic tomography of the proton Bragg peak in combination with ultrasound and optoacoustic imaging," *Scientific Reports*, vol. 6, p. 29305, 2016.

[71] K. Jones, W. Nie, J. Chu, J. Turian, A. Kassaee, C. M. Sehgal, and S. Avery, "Acoustic-based proton range verification in heterogeneous tissue: simulation studies," *Physics in Medicine and Biology*, vol. 63, no. 2, p. 025018, 2018.

[72] T. Kundu, "Acoustic source localization," *Ultrasonics*, vol. 54, no. 1, pp. 25–38, 2014.

[73] M. Dierolf, A. Menzel, P. Thibault, P. Schneider, C. M. Kewish, R. Wepf, O. Bunk, and F. Pfeiffer, "Ptychographic X-ray computed tomography at the nanoscale," *Nature*, vol. 467, no. 7314, pp. 436–439, 2010.

[74] K. J. Gaffney and H. N. Chapman, "Imaging atomic structure and dynamics with ultrafast X-ray scattering," *Science*, vol. 316, no. 5830, pp. 1444 – 1448, 2007.

[75] J. Miao, T. Ishikawa, I. K. Robinson, and M. M. Murnane, "Beyond crystallography: Diffractive imaging using coherent x-ray light sources," *Science*, vol. 348, no. 6234, pp. 530 – 535, 2015.

[76] R. Neutze, R. Wouts, D. van der Spoel, E. Weckert, and J. Hajdu, "Potential for biomolecular imaging with femtosecond X-ray pulses," *Nature*, vol. 406, pp. 752–757, 2000.

[77] A. L. Robinson, "High-resolution imaging with soft x-rays," *Science*, vol. 215, no. 4529, pp. 150 – 152, 1982.

[78] A. L. Robinson, "Imaging unaltered cell structures with x-rays," *Science*, vol. 237, no. 4816, pp. 723 – 724, 1987.

[79] J. A. Rowlands, "Material change for X-ray detectors," *Nature*, vol. 550, p. 47, 2017.

[80] C. G. Schroer, "X-ray imaging: The chemistry inside," *Nature*, vol. 476, p. 159, 2011.

[81] R. F. Service, "Brilliant X-rays Reveal Fruits of a Brilliant Mind," *Science*, vol. 313, no. 5788, p. 744, 2006.

[82] M. Tegze, G. Faigel, S. Marchesini, M. Belakhovsky, and O. Ulrich, "Imaging light atoms by X-ray holography," *Nature*, vol. 407, p. 38, 2000.

[83] A. L. Robinson, "Image Reconstruction (I): Computerized X-Ray Scanners," *Science*, vol. 190, no. 4214, pp. 542 – 593, 1975.

[84] E. C. Lin, "Radiation risk from medical imaging," *Mayo Clinic Proceedings*, vol. 85, no. 12, pp. 1142–1146, 2010.

[85] J. B. Hobbs, N. Goldstein, K. E. Lind, D. Elder, G. D. Dodd, and J. P. Borgstede, "Physician knowledge of radiation exposure and risk in medical imaging," *Journal of the American College of Radiology*, vol. 15, no. 1, pp. 34–43, 2018.

[86] L. Xiang, S. Tang, M. Ahmad, and L. Xing, "High resolution x-ray-induced acoustic tomography," *Scientific Reports*, vol. 6, p. 26118, 2016.

[87] S. Tang, D. H. Nguyen, A. Zarafshani, C. Ramseyer, B. Zheng, H. Liu, and L. Xiang, "X-ray-induced acoustic computed tomography with an ultrasound transducer ring-array," *Applied Physics Letters*, vol. 110, no. 10, p. 103504, 2017.

[88] D. P. Umstadter, "All-laser-driven Thomson X-ray sources," *Contemporary Physics*, vol. 56, no. 4, pp. 417–431, 2015.

[89] S. Chen, G. Golovin, C. Miller, D. Haden, S. Banerjee, P. Zhang, C. Liu, J. Zhang, B. Zhao, S. Clarke, S. Pozzi, and D. Umstadter, "Shielded radiography with a laser-driven MeV-energy

942   X-ray source," *Nuclear Instruments and Methods in Physics Research Section B: Beam Inter-*

943   *actions with Materials and Atoms*, vol. 366, pp. 217–223, 2016.

944 [90] S. Tang, K. Yang, Y. Chen, and L. Xiang, "X-ray-induced acoustic computed tomography for

945   3D breast imaging: A simulation study," *Medical Physics*, vol. 0, no. 0, 2018.

946 **X. FIGURE CAPTIONS**

947 **Fig. 1.** CT scan and treatment plan of a hepatic patient undergoing proton radiotherapy.
948 The arrow represents the position of the hydrophone, and the detected acoustic signal is
949 superimposed onto the CT scan. The faint red lines represent isodose curves of the planned
950 dose distribution. Reprinted with permission from [29].

951 **Fig. 2.** Schematic demonstrating the propagation and detection of induced acoustic waves.
952 The black dots represent point pressure sources, and the dotted lines represent the resulting
953 pressure waves. Different colours represent the position of the induced acoustic wave at
954 subsequent times following irradiation. More complicated pressure distributions can be
955 treated as the superposition of many point sources. The dashed circles surrounding each
956 transducer represent the transducer detection surfaces, with each colour corresponding to a
957 different detection time equal to the distance from the transducer divided by the speed of
958 sound in the medium.

959 **Fig. 3.** (a) Block diagram of a puzzle piece shaped radiation field, where white regions
960 represent the primary radiation beam. (b) Experimental and (c) simulated XACT images
961 of the field. (d) Comparison of profiles extracted from experimental and simulated XACT
962 images to ion chamber measurements along the X-axis at Y= -15 mm. Reproduced with
963 permission from [36].

964 **Fig. 4.** (a) CT scan with the overlaid dose distribution for a lateral beam extracted from
965 a VMAT delivery. The simulated transducer is placed at the perineum. (b) The transducer
966 signal mapped into distance and compared to the dose profile along the detection line. Each
967 boundary generates a bipolar pulse, and the transition between the two components of each
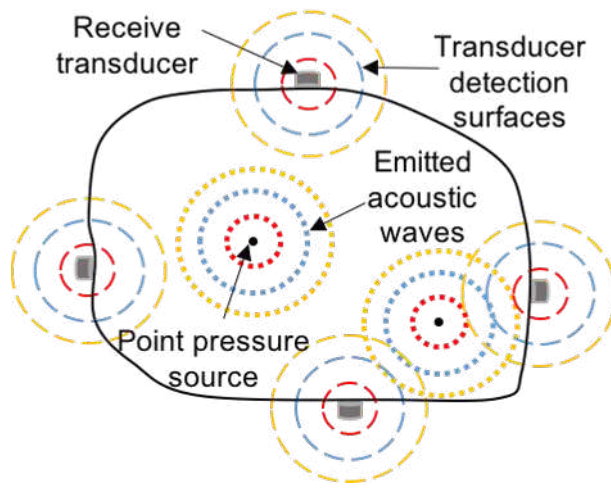968 pulse aligns with the dose gradient.

969 **Fig. 5.** Variation of repeated ionoacoustic range measurements at several energies, com-
970 pared to a fit of existing Stingray data. For 200.21 MeV, Stingray range value was measured
971 consecutively to the ionoacoustic data acquisition. Reproduced with permission from [16].

Fig. 6. First time triple-modality imaging of a mouse leg using (a) optoacoustics, (b) ultrasonography, (c) ionoacoustics in red marking the Bragg peak location and coregistered to the optoacoustics image. (d) A cryoslice of the mouse leg, where the star indicates the medial marginal vein. The scale in figures (a) and (b) represents 2 mm. Reprinted with permission from [70].
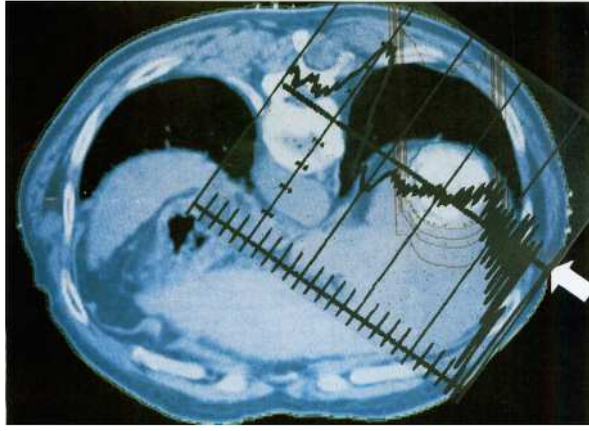
Fig. 7. The acoustic waves induced by a single proton pencil beam were simulated in a 3D CT liver volume (a transverse slice is shown at left). To characterize the effects of heterogeneity, the acoustic waves were propagated in water, a homogeneous tissue volume, and a heterogeneous tissue volume. Pressure traces simulated at detector position 6 are overlaid onto the images. Reproduced with permission from [71].

Fig. 8. Schematic diagram of XACT imaging system. A scintillator/photodiode combination is activated by the X-rays and is used to trigger the data receiver to start collecting signals from the ultrasound transducer array. Reprinted with permission from [87].

Fig. 9. (a) Gold fiducial marker XACT image. Reprinted with permission from [86]. (b) Lead OU logo XACT image. Reprinted with permission from [87].

Receive transducer

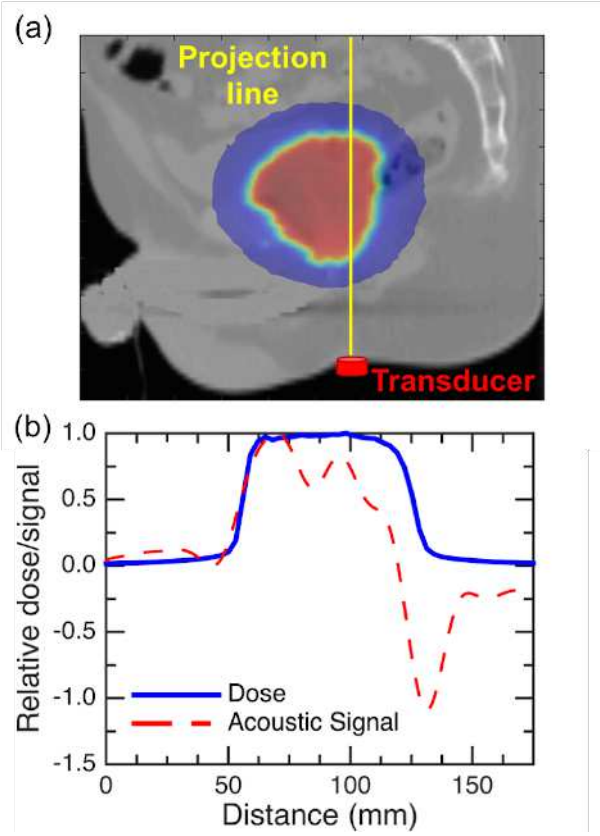Transducer detection surfaces

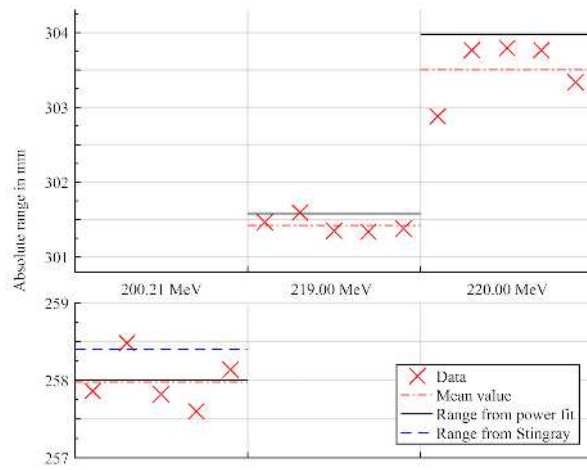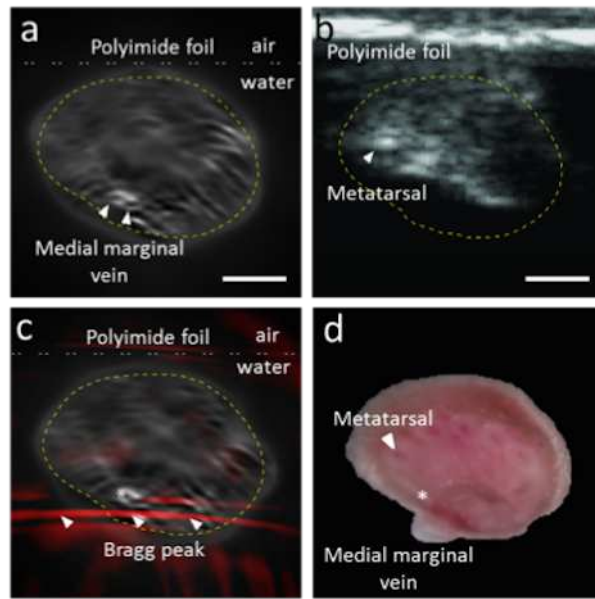Emitted acoustic waves

Point pressure source
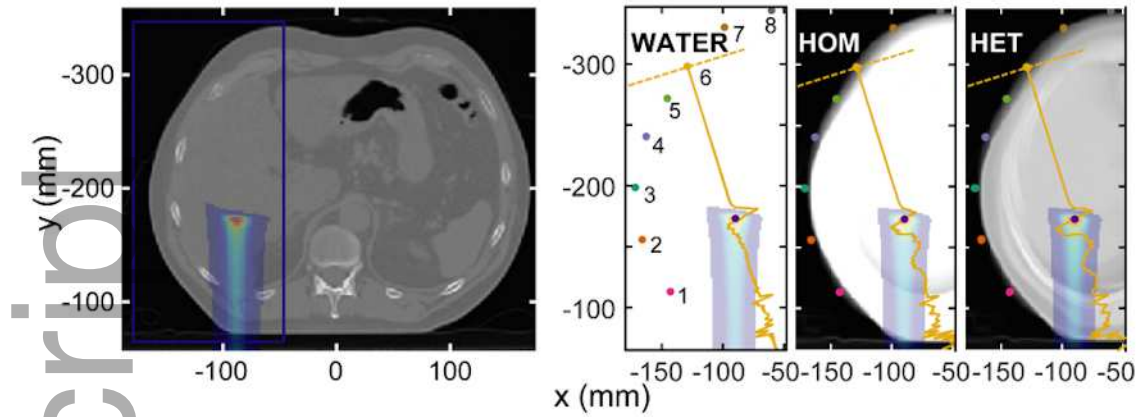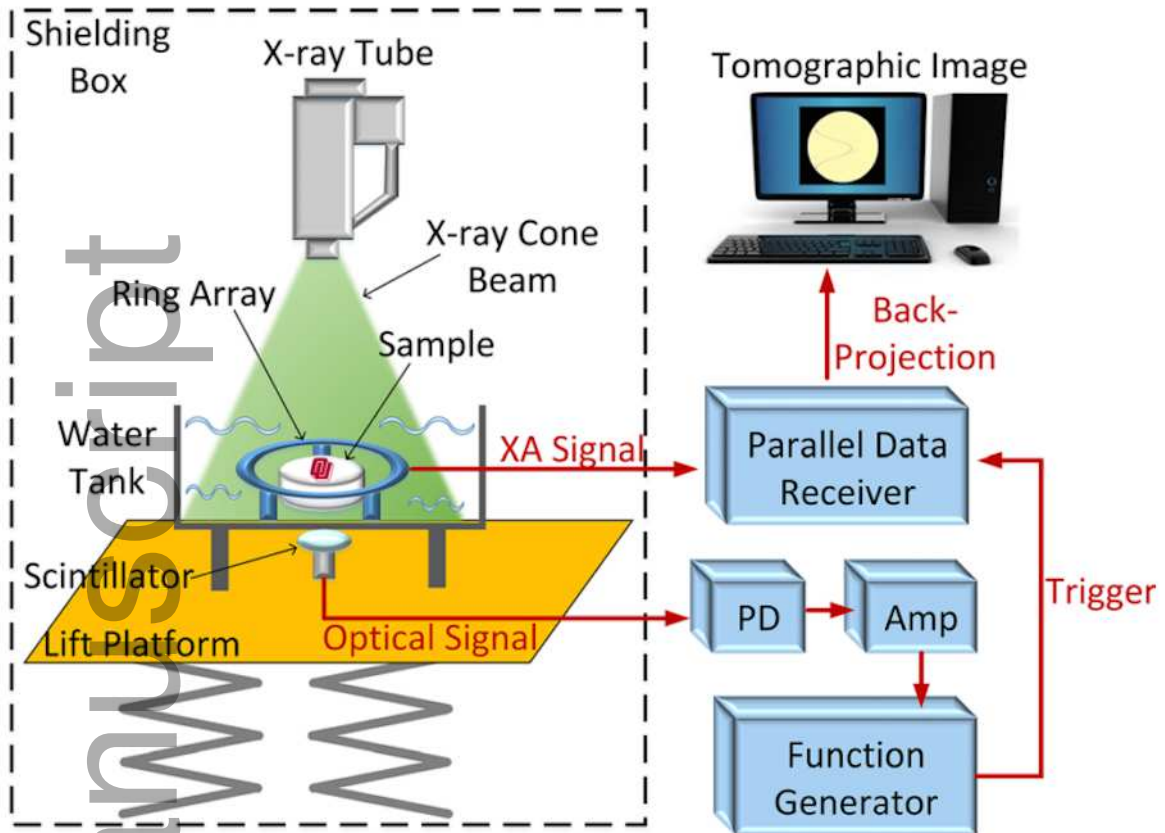
mp_12929_f1.tif

mp_12929_f2.tif
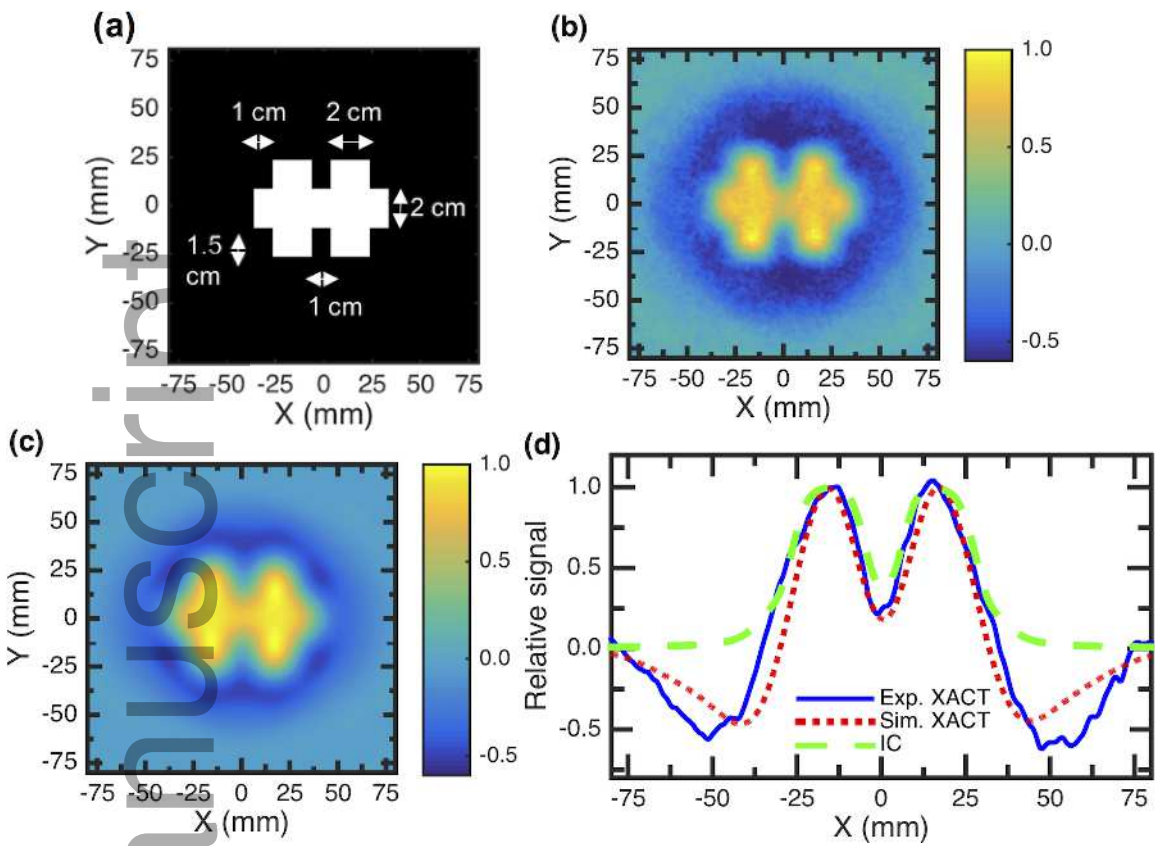
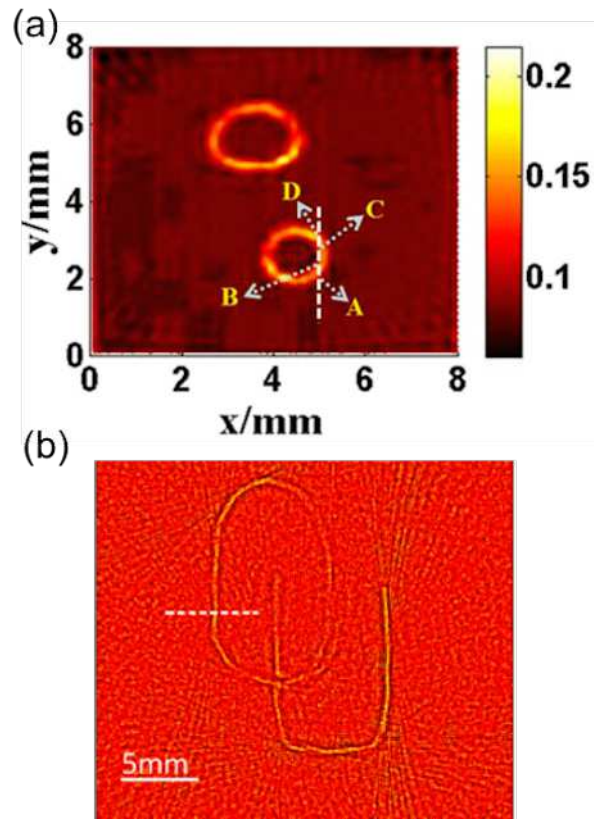mp_12929_f3.tif

mp_12929_f4.tif

mp_12929_f5.tif

mp_12929_f6.tif

mp_12929_f7.tif

mp_12929_f8.tif

mp_12929_f9.tif